Resolving the 3D rotational and translational dynamics of single molecules using radially and azimuthally polarized fluorescence

Oumeng Zhang,[†] Weiyan Zhou,[†] Jin Lu,[†] Tingting Wu,[†] and Matthew D. Lew[*,†,‡,¶]

[†]Department of Electrical and Systems Engineering
[‡]Center for the Science and Engineering of Living Systems
[¶]Institute of Materials Science and Engineering, Washington University in St. Louis, Missouri 63130, USA

E-mail: mdlew@wustl.edu

Abstract

We report a radially and azimuthally polarized (raPol) microscope for high detection and estimation performance in single-molecule orientation-localization microscopy (SMOLM). With 5000 photons detected from Nile red (NR) transiently bound within supported lipid bilayers (SLBs), raPol SMOLM achieves 2.1 nm localization precision, 1.4° orientation precision, and 0.15 sr precision in estimating rotational wobble. Within DPPC SLBs, SMOLM imaging reveals the existence of randomly oriented binding pockets that prevent NR from freely exploring all orientations. Treating the SLBs with cholesterol-loaded methyl-β-cyclodextrin (MβCD-chol) causes NR's orientational diffusion to be dramatically reduced, but curiously, NR's median lateral displacements drastically increase from 20.8 nm to 75.5 nm (200 ms time lag). These jump diffusion events overwhelmingly originate from cholesterol-rich nanodomains within the SLB. These detailed measurements of single-molecule rotational and translational dynamics are made possible by raPol's high measurement precision and are not detectable in standard SMLM.

Beyond improving the localization accuracy[1–6] of single-molecule localization microscopy (SMLM),[7–10] simultaneously imaging molecular positions and orientations in single-molecule orientation localization microscopy (SMOLM) provides unparalleled insights into biochemical processes. Recent developments in SMOLM allow scientists to resolve the organization of amyloid aggregates,[11–13] conformations of DNA strands,[6,14–18] and the structure of actin networks.[19–21] Using point spread function (PSF) engineering, microscopists have developed various techniques[4,6,20,22,23] to improve measurement precision, approaching the fundamental performance limits for measuring both orientation[24–26] and localization.[27,28]

However, many SMOLM techniques exhibit poor measurement precision for molecules that are oriented out of the coverslip plane (e.g., the x- and y-polarized (xyPol) standard PSF[12,29]). Others improve measurement precision by expanding the imaging system PSF significantly and thus suffer degraded localization precision and detection sensitivity for dim emitters (e.g., the Tri-spot PSF[22]). Despite the recent developments of CHIDO[20] and the vortex PSF[6] for imaging the 3D positions and orientations of single molecules (SMs), no existing techniques exhibit sufficiently high localization precision, orientation precision, and sensitivity to SM wobble for simultaneous 3D orientation, wobble, and posi-

tion tracking of SMs within lipid membranes. Inspired by symmetries within the dipole radiation pattern, we demonstrate a highly sensitive and easy to implement SMOLM technique using radially and azimuthally polarized (raPol) fluorescence,[24,26,30] a variant of the y-Phi PSF.[5] It is implemented using a commercially available vortex (half) wave plate (VWP) and polarizing beamsplitter (PBS) within a widefield epifluorescence microscope. Unlike other techniques, the orientation estimation performance of the raPol microscope is excellent for molecules oriented along the optical axis (out of the coverslip plane). We utilize the raPol PSF to study the dynamics of Nile red (NR) molecules transiently bound to supported lipid bilayers (SLBs).[31] Imaging NR dynamics within DPPC SLBs reveals the existence of randomly oriented binding pockets that prevent NR from freely rotating. In addition, raPol is capable of tracking simultaneously the position and orientation of NR as it explores SLBs modified by methyl-β-cyclodextrin loaded with cholesterol (MβCD-chol). As cholesterol (chol) is deposited, NR's orientation tilts mostly perpendicular to the SLB, and its rotational diffusion is greatly reduced, but its translational diffusion dramatically increases almost four-fold. These data suggest that NR "jumps" between cholesterol-rich nanodomains within the SLB. To our knowledge, these experiments are the first measurements of how MβCD-chol affects the nanoscale chemical environments within lipid membranes at the single-molecule level.

We begin by describing a rotationally diffusing molecule using its average orientation $\boldsymbol{\mu} = [\mu_x, \mu_y, \mu_z]^{\dagger} = [\sin\theta\cos\phi, \sin\theta\sin\phi, \cos\theta]^{\dagger}$ within a hard-edged cone of solid angle Ω (Figure 1a), where μ_z is parallel to the optical axis, $\Omega = 0$ represents a rotationally-fixed molecule, and $\Omega = 2\pi$ represents a freely-wobbling molecule. Here, we assume that the SM wobbles uniformly within the cone for simplicity, and our analysis may be easily adapted for other rotational potential wells or geometries.[32–34]

Due to the symmetry of the dipole emission pattern, the photons emitted by an SM oriented parallel to the optical axis ($\mu_z = 1$) captured by an objective lens are radially polarized.[3,35,36] Therefore, an intuitive way to distinguish out-of-plane molecules from in-plane ones is to measure radially vs. azimuthally polarized fluorescence. We achieve this polarization separation by adding a VWP (Figure 1b) to the back focal plane (BFP) of a microscope with two polarized imaging channels. The spatially-varying fast axis direction of the VWP turns the radially and azimuthally polarized light to x and y-polarized light. A PBS is then used to separate the fluorescence into radially and azimuthally polarized

images (Figure S1a). As a molecule rotates out of plane, i.e., as μ_z increases, photons shift from the azimuthally polarized to the radially polarized channel. When the SM is aligned with the optical axis, all fluorescence photons are confined to the radially polarized image (Figure 1c, red).
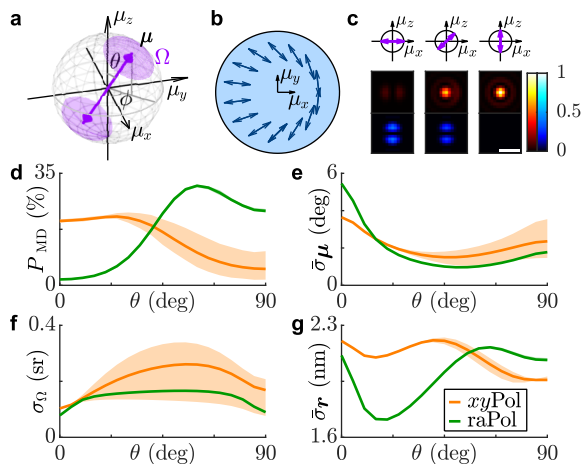

Figure 1: The radially and azimuthally polarized (raPol) standard PSF. (a) The rotational diffusion of a fluorescent molecule is described using a unit vector $\boldsymbol{\mu}$ and a wobble solid angle Ω on the surface of a hard-edged cone. (b) A vortex (half) waveplate (VWP) is placed at the back focal plane of the imaging system, transforming radially and azimuthally polarized light to x and y-polarized light, respectively. Arrows represent the VWP's fast axis. (c) Representative radially (red) and azimuthally (blue) polarized PSFs of rotationally-fixed molecules with polar angles θ of $90°$, $45°$, and $0°$. Colorbar: normalized intensity. Scale bar: 500 nm. (d) The probability of a missed detection P_{MD} (i.e., a false negative) for 250 signal photons detected from an SM with fixed wobble $\Omega = 0.28\pi$ sr and various polar angles θ. These probabilities were computed using a Monte Carlo simulation of 25,000 noisy images. The best-possible precision for estimating the (e) average orientation $\boldsymbol{\mu}$, (f) wobble angle Ω, and (g) 2D position $\boldsymbol{r}$ of an SM with 5000 signal photons detected based on the Crámer-Rao bound. Orange: xyPol; green: raPol. Solid lines represent the mean precision averaged over all azimuthal angles ϕ; shaded areas represent the minimum to maximum range of precisions at each polar angle θ. The background is 30 photons per camera pixel $(66.86 \times 66.86 \text{ nm}^2)$.

High detection rates are critical for collecting unbiased measurements of SM dynamics. We quantify the missed detection (false negative) rate P_{MD} of raPol compared to xyPol, a common easy-to-implement SMOLM technique, using binary detection theory[37] (SI Section 2.1). Note that due to the complexity of jointly detecting and localizing molecules in SMLM and SMOLM, the theoretical rate P_{MD} is overly optimistic compared to practical algorithmic performance and should be interpreted as an estimate of relative performance between PSFs. For a low signal-to-background ratio (SBR), we find that the detection performance of raPol is comparable to that of xyPol (Figure 1d). Thus, dim SMs are detected more reliably using raPol as opposed to most engineered PSFs optimized for SMOLM; it is more difficult to detect weak emitters using larger PSFs. Due to the toroidal, polarized emission pattern of an SM, detection performance is orientation-dependent. For z-oriented molecules, the miss

rate using raPol is 80% less than that of xyPol since the energy is concentrated in the radially polarized channel, but worse for in-plane molecules for the opposite reason (Figure 1c). Intuitively, the missed detection rate decreases as the peak intensity of the PSF increases (Figure S2b,c). Interestingly, due to the symmetry of raPol, its detection performance is not affected by the azimuthal angle ϕ, whereas that of xyPol may vary up to a factor of 6 across various ϕ (Figure S2a,b).

Next, we compare the best-possible orientation and position measurement precision for raPol and xyPol using the Cramér-Rao bound (CRB, SI Section 2.2).[37] The precision of measuring the average orientation $\bar{\sigma}_{\boldsymbol{\mu}}$ is quantified as the angle subtended by an arc that represents measurement uncertainty on the orientation unit sphere (SI Section 2.2). Strikingly, raPol exhibits superior orientation measurement precision over xyPol for 91.0% of all possible SM orientations (Figure 1e and Figure S2e). Similarly, for 83.8% of all possible orientations, raPol measures SM wobble more precisely than xyPol does (Figure 1f and Figure S2f). Notably, the average 2D localization precision $\bar{\sigma}_{\boldsymbol{r}}$ using raPol is also slightly better than that of xyPol (Figure 1g and Figure S2d, 2.6% improvement), even though xyPol is usually perceived to be optimal for localizing in-focus molecules.

While the translational dynamics of fluorophore-lipid interactions have been characterized at the SM level, e.g., by fluorescence correlation spectroscopy,[38] relatively little is known about their rotational dynamics. We next study the rotational dynamics of Nile red within SLBs[31] using points accumulation for imaging in nanoscale topography (PAINT).[10] We form a DPPC [di(16:0)PC (phosphatidylcholine), Figure S4] bilayer on coverglass and use RoSE-O, a sparsity-promoting maximum-likelihood estimation algorithm,[18] to analyze images of blinking NR molecules and extract their positions and orientations. First, we measure NR within a DPPC SLB using both xyPol and raPol, excited by circularly polarized epi (Figure 2a) and total internal reflection fluorescence (TIRF, Figure 2d) illumination. Interestingly, NR's polar orientation θ changes significantly with illumination polarization, from a median of $\tilde{\theta}_{\mathrm{epi,raPol}} = 80.4°$ to $\tilde{\theta}_{\mathrm{TIRF,raPol}} = 41.6°$, implying that NR's emission dipole orientation is correlated with the orientation of its absorption dipole moment within a DPPC SLB. To confirm, we changed the laser beam tilt to $\alpha = 25°$ and $\alpha = 45°$ relative to the optical axis (Figure 2b,c). As the z-polarized electric field in the excitation beam increased, the observed NR polar angles systematically decreased ($\tilde{\theta}_{\alpha=25°} = 74.4°$, $\tilde{\theta}_{\alpha=45°} = 57.7°$). The change in polar angle is obvious within the raPol images at each illumination angle α; fluorescence photons become increasingly radially polarized as α increases [Figure 2(i)]. These trends were consistently observed across ~35k localizations and 12 fields of view.

To explain how the polarization of the illumination laser strongly affects the observed NR orientations, we used Monte Carlo simulations to model light absorption, rotational diffusion,[39,40] and photon emission of NR within a DPPC SLB, using reported values for its excited-state lifetime (4.6 ns) and rotational diffusion coefficient (0.035 $\mathrm{rad}^2/\mathrm{ns}$).[41] These simulations generate images of diffusing SMs (SI Section 4.1), and we use RoSE-O to obtain measurements of their average orientation ($\theta_{\mathrm{sim}}, \phi_{\mathrm{sim}}$) and rotational wobble Ω_{sim} (Figure 2e,f). To best match the experimental orientation measurements, we allow each NR to have a random average orientation $\boldsymbol{\mu}_{\mathrm{sim}}$ uniformly distributed within the domain $|\mu_{z,\mathrm{sim}}| > 0.1$. Each SM also has a random
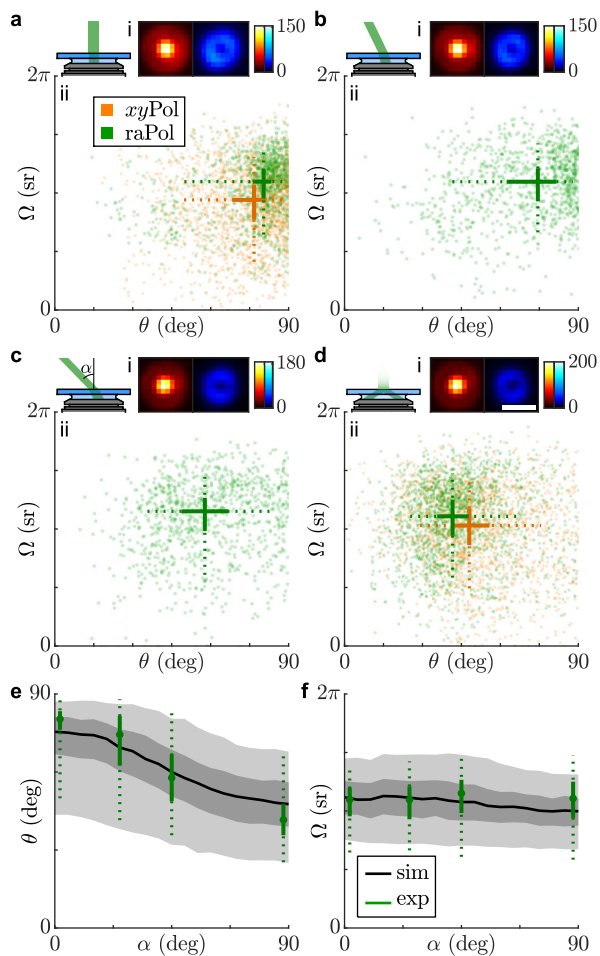
Figure 2: Rotational diffusion of Nile red (NR) within DPPC supported lipid bilayers (SLBs). (a-d) (i) Average raPol images and (ii) orientation and wobble measurements of NR as a function of illumination tilt angle α: (a) $0°$, (b) $25°$, (c) $45°$, and (d) total internal reflection fluorescence (TIRF). Measurements were collected using both (orange) xyPol and (green) raPol imaging. Crosses represent the median of the distribution, while solid lines represent the 33rd and 67th percentiles, and dotted lines represent the 10th and 90th percentiles. (e,f) Quantifying the effect of illumination tilt angles α on measurements of (d) polar angle θ and (e) wobble Ω. Green: experimental measurements. Dots represent the median, solid lines represent 33rd and 67th percentile, and dotted lines represent the 10th and 90th percentile. Black and gray: simulated orientation measurements of rotationally diffusing SMs, assuming an excited-state lifetime of 4.6 ns, rotational diffusion coefficient of 0.035 rad^2/ns, and constrained diffusion within a hard-edged cone of solid angle $\Omega_{\text{sim}} \in [0.7\pi, 1.7\pi]$ sr. Lines, dark and light gray areas represent the median, 33rd/67th, and 10th/90th percentiles, respectively. Colorbar: photons; scalebar: 500 nm.

wobble within a hard-edged cone of solid angle Ω_{sim} uniformly distributed between 0.7π and 1.7π; a molecule can freely explore all possible orientations within the aforementioned cone. With these parameters, the simulated orientation measurements match both the experimental median and variation in NR orientations reasonably well (7.8% average error in median $\tilde{\theta}$, 5.0% average error in median $\tilde{\Omega}$).

Our model therefore suggests that during a fluorescence

"flash," NR embeds itself within a network of binding pockets between lipid acyl chains; some are stable on the order of our camera exposure time (100 ms), while others rotate slowly over ~1 sec (see below). These anisotropic pockets are randomly oriented in all directions except parallel to the coverslip (i.e., $\theta \in [0°, 84°]$). Further, steric effects allow NR to explore an intermediate range of orientations (median $\tilde{\Omega} = 1.11\pi$ sr in our experiments irrespective of illumination tilt α) but prevent it from rotating freely.
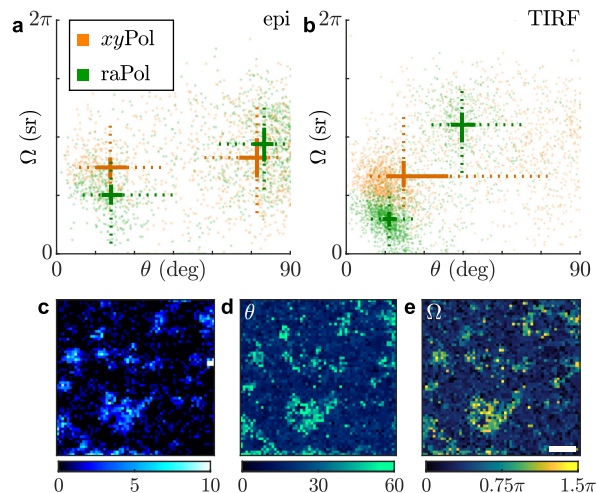

Figure 3: Orientation distribution of NR molecules within DPPC SLBs after cholesterol-loaded methyl-β-cyclodextrin (MβCD-chol) treatment excited by (a) epi and (b) TIRF illumination and measured using (orange) xyPol and (green) raPol. Crosses represent the median of the distribution, while solid lines represent the 33rd and 67th percentiles, and dotted lines represent the 10th and 90th percentiles. A k-means clustering ($k = 2$) is used to separate the distribution into two populations. (c-e) Identifying cholesterol-rich regions within the SLB using raPol and TIRF illumination. (c) SMLM image of NR in the azimuthally polarized imaging channel. (d-e) SMOLM images of (d) median polar angle θ and (e) median wobble cone angle Ω of NR localizations in each bin. Colorbars: (c) localizations per bin, (d) polar angle (deg), (e) wobble solid angle (sr). Bin size: 100×100 nm^2. Scale bar: 1 µm.

We next explore raPol's ability to detect chol-induced ordering within DPPC SLBs.[31] Cholesterol is loaded into the bilayer using two successive MβCD-chol treatments (40 µM for 5 minutes, then 80 µM for 5 minutes, SI Section 3.2), and we again measured NR orientations using xyPol and raPol under epi (Figure 3a) and TIRF excitation (Figure 3b). We observe two distinct "clusters" of NR orientations under both illumination conditions; the first is oriented nearly perpendicular to the SLB (median $\tilde{\theta}_{\text{TIRF,raPol,1}} = 16.5°$), which is consistent with previous observations.[31] The polar angles of localizations within this cluster do not change with illumination polarization, except that number of localizations when using epi illumination is 15% of that using TIRF. Both xyPol and raPol detect a decrease in rotational wobble (median $\tilde{\Omega}_{\text{TIRF,raPol,1}} = 0.93$ sr) when chol is present. These data suggest that this population of NR is tightly confined within a small range of orientations during its fluorescence lifetime, which is consistent with our intuition of increased crowding within chol-condensed SLBs.

However, we note a significant discrepancy between xyPol

and raPol measurements of the second cluster. When using raPol, this other population of NR exhibits similar orientations (median $\tilde{\theta}_{\text{TIRF,raPol,2}} = 44.5°$, $\tilde{\Omega}_{\text{TIRF,raPol,2}} = 3.47$ sr) to that of NR within the DPPC-only SLB (Figure 2a, $\tilde{\theta}_{\text{TIRF,raPol}} = 41.6°$, $\tilde{\Omega}_{\text{TIRF,raPol}} = 3.48$ sr). However, there is no clearly resolved second cluster in the xyPol measurements, just a long tail in the $\theta - \Omega$ distribution [Figure S8a(i)]. Compared to raPol imaging (Figure 1e,f and Table S2), xyPol's degraded orientation sensitivity makes it difficult to resolve these two NR orientation behaviors within DPPC-chol SLBs.

These two distinct orientation subpopulations raise the question: are these NR binding behaviors uniformly dispersed throughout the SLB, or has chol partitioned the SLB into micro- or nanodomains? We first use ThunderSTORM to localize NR blinking events in the azimuthally polarized channel. Since NR within ordered DPPC-chol SLBs is nearly fixed and perpendicular to the membrane (Figure 3b), azimuthally polarized fluorescence only originates from regions of the SLB that are depleted of cholesterol. We observe an obvious distinction between darker cholesterol-rich regions vs. localization hotspots without cholesterol (Figure 3c). Analyzing images from both raPol channels using RoSE-O, we are able to construct SMOLM orientation θ (Figure 3d) and wobble Ω (Figure 3e) images, where chol-depleted nanodomains are easy to distinguish due to their large polar and wobble angles. These regions are difficult to detect in standard SMLM reconstructions since NR's localization density is mostly uniform everywhere (Figure S8d). Interestingly, xyPol is able to distinguish between chol-rich and poor regions of the SLB using NR polar angles θ (Figure S8b), but its map of NR wobble Ω is extremely noisy (Figure S8c).

With increasing chol in the SLB, we also observed remarkable changes in the residence time of many NR molecules. Here, we track the 2D positions and 3D orientations simultaneously of diffusing NR molecules over multiple frames (see Figure S11d for the distribution of NR binding times). Within the DPPC-only SLB, one molecule is translationally fixed, but rotates along the polar direction; the brightness ratio between the raPol imaging channels changes over time (Figure 4a-c, blue). After a single application of MβCD-chol, another SM exhibits more translational diffusion and rotates along the azimuthal direction; the double-spot PSF in the azimuthally polarized channel rotates dramatically over time (Figure 4a-c, orange). After the final treatment, another NR molecule moves a large distance in x and y but remains z-oriented throughout its entire trajectory (Figure 4a-c, purple). Additional representative SM trajectories are shown in Figure S9.

To quantify rotational diffusion between frames, we compute the angular displacement (i.e., rotation) of single NR as

$$\delta_i = \cos^{-1}(\boldsymbol{\mu}_{i+1} \cdot \boldsymbol{\mu}_i), \tag{1}$$

which represents an angle between two adjacent orientation measurements $\boldsymbol{\mu}_i$ and $\boldsymbol{\mu}_{i+1}$ within an SM trajectory. This slow-scale displacement remains unchanged after a first application of MβCD-chol [27.3° ± 26.5° (median ± std. dev.) before and 26.4° ± 25.7° after treatment, respectively, Figure 4d]. Only after a second higher-dose incubation of MβCD-chol does the average SM rotation $\bar{\delta}$ decrease to 20.3° ± 20.2°. In contrast, fast-scale intraframe SM wobbling Ω decreases successively after each treatment (Figure 4d), from 3.93 ± 0.96 sr before treatment to 3.24±1.05 sr after a 40 μM incubation for 5 min., and finally to 1.74 ± 1.06 sr after a 80 μM treatment.
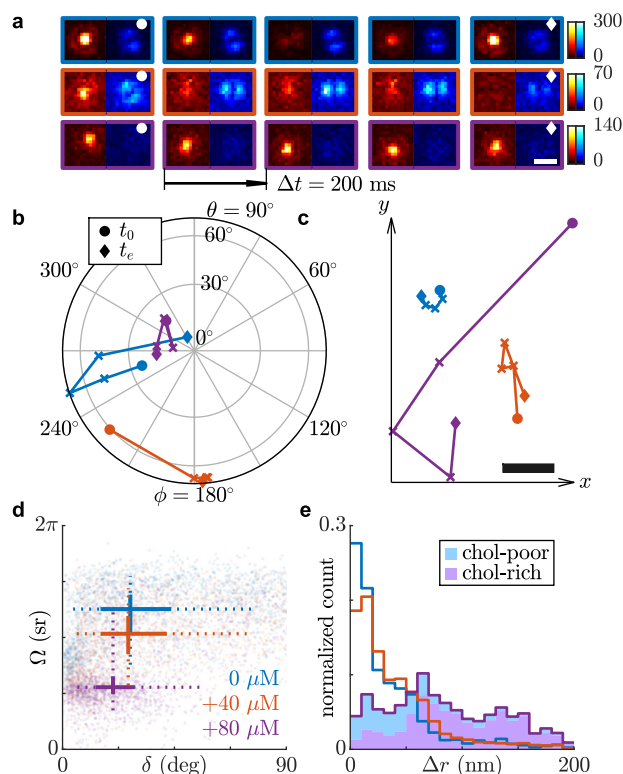

Figure 4: Rotational and translational dynamics of NR within SLBs before and after successive MβCD-chol treatments. (a) Raw raPol images of three SMs undergoing diffusion. Scale bar: 500 nm; colorbar: photons. (b,c) SM trajectories exhibiting (b) rotational and (c) translational diffusion corresponding to images in (a). Circles and diamonds represent the first (t_0) and last frame (t_e), respectively. The relative position between the three trajectories in (c) is arbitrary. Scale bar: 50 nm. (d) Average angular displacement $\bar{\delta}$ vs. average wobble Ω for each NR trajectory. Solid lines represent the 33rd and 67th percentile, and dotted lines represent the 10th and 90th percentile of each distribution. Intersections represent the median. (e) Measured lateral displacements Δr accumulated over all NR trajectories. Shaded area (purple) represents localizations within chol-rich regions of the SLB, as measured by the NR polar angle θ and wobble Ω. Blue: before MβCD-chol treatment; orange: after 40 μM treatment for 5 minutes; purple: after 80 μM treatment for 5 minutes. All data here are from blinking events lasting at least two consecutive frames (200 ms).

Even though NR molecules become more rotationally constrained as chol concentration increases, they curiously exhibit successively larger translational motions. The lateral displacement, given by

$$\Delta r_i = \|\boldsymbol{r}_{i+1} - \boldsymbol{r}_i\|, \tag{2}$$

is 20.8 ± 37.4 nm (median ± std. dev., 200 ms time lag between the ith and $(i + 1)^{\text{th}}$ frame) averaged across all NR localizations before adding MβCD-chol (Figure 4e). After a 40 μM treatment, the average displacement becomes 28.2 ± 37.5 nm and grows to 75.5 ± 50.3 nm after a 80 μM treatment. We gain additional insight into these behaviors by using the polar orientation θ and wobble Ω of each localization to separate molecules exploring chol-rich regions

of the SLB from those exploring chol-poor ones (using k-means classification, see SI Section 4.3). We find that the largest lateral displacements overwhelmingly occur when NR is within chol-rich domains [$\Delta r = 44.4 \pm 44.1$ nm in chol-poor vs. $\Delta r = 91.5 \pm 47.1$ nm in chol-rich domains, Figure S10c(iii)]. In fact, the proportion of all large lateral displacements ($\Delta r > 62.4$ nm = 3× the median of Δr in DPPC SLBs) that originate from chol-rich regions is more than 84.8%.

In summary, we design and implement a new PSF, the radially and azimuthally polarized (raPol) standard PSF, for SMOLM that only requires a commercially available waveplate and polarizing beamsplitter to be added to a standard epifluorescence microscope. The PSF is significantly more compact than other engineered PSFs. Despite its compactness, raPol's orientation precision is 30.6% better on average compared to xyPol. In addition, since z-oriented dipoles produce radially polarized light, raPol can directly detect the presence of out-of-plane molecules via a simple quantification of the brightness ratio between its two detection channels (Figure 3c). Thus, it achieves excellent sensitivity for measuring the polar orientation of a fluorescent molecule.[25,26]

This combination of superior detection rate, excellent orientation measurement precision, and strong localization precision enables raPol to measure the rotational and translational dynamics of SMs with exquisite detail. For example, after a first dose of MβCD-chol, the average cholesterol concentration within the membrane is still relatively low (Figure S7b), but by measuring the decreasing wobble Ω, we can detect the changing chemical composition of the SLB. After a second treatment, we find that NR demonstrates a curious combination of diffusive behaviors: strongly confined rotational motions but dramatically larger translational jumps between frames. The distribution of lateral displacements Δr (Figure 4e, purple) is non-exponential and broad, and thus, NR diffusion is inhomogeneous throughout the SLB. We surmise that the MβCD-chol treatments dissolve the SLB in a highly nonuniform manner, causing NR to exhibit "jump diffusion" between regions of intact membrane. NR molecules repeatedly diffuse across damaged portions of the bilayer with widely varying jump distances Δr to bind transiently with other chol-rich islands, where their orientations are highly confined upon binding. Thus, NR's rotational and translational dynamics, as observed by raPol SMOLM, support previous observations of cyclodextrin molecules damaging lipid membranes by carrying away lipid molecules after depositing cholesterol.[42,43] This insight into MβCD-chol activity on the SLB is not detectable by conventional SMLM (Figure S8d,e). These observations demonstrate that imaging SM positions and orientations simultaneously is powerful for elucidating a more complete picture of chemical dynamics at the nanoscale.

Looking ahead, we anticipate that the ease of implementing raPol will enable SMOLM to be adopted more widely by the nanoscience community. Further developments are needed in image analysis technologies to increase their automation, robustness, and speed. The excellent detection rate, measurement precision, and simple optical setup of raPol makes it a robust tool for studying a variety of dynamics and processes in soft matter with SM sensitivity and nanoscale resolution.

Supporting Information Available

Imaging system schematic and alignment and calibration procedures; characterization of raPol's detection and estimation performance; additional NR orientation-localization analysis; additional references.[44] The data underlying this study are openly available in OSF at `https://osf.io/64bfv/?view_only=3a2cbdc3fd20467486f3574d54ecc7f6` and from the corresponding author upon reasonable request.

References

(1) Engelhardt, J.; Keller, J.; Hoyer, P.; Reuss, M.; Staudt, T.; Hell, S. W. Molecular Orientation Affects Localization Accuracy in Superresolution Far-Field Fluorescence Microscopy. *Nano Letters* **2011**, *11*, 209–213.

(2) Backlund, M. P.; Lew, M. D.; Backer, A. S.; Sahl, S. J.; Grover, G.; Agrawal, A.; Piestun, R.; Moerner, W. E. Simultaneous, accurate measurement of the 3D position and orientation of single molecules. *Proceedings of the National Academy of Sciences* **2012**, *109*, 19087–19092.

(3) Lew, M. D.; Moerner, W. E. Azimuthal Polarization Filtering for Accurate, Precise, and Robust Single-Molecule Localization Microscopy. *Nano Letters* **2014**, *14*, 6407–6413.

(4) Backlund, M. P.; Lew, M. D.; Backer, A. S.; Sahl, S. J.; Moerner, W. E. The Role of Molecular Dipole Orientation in Single-Molecule Fluorescence Microscopy and Implications for Super-Resolution Imaging. *ChemPhysChem* **2014**, *15*, 587–599.

(5) Backlund, M. P.; Arbabi, A.; Petrov, P. N.; Arbabi, E.; Saurabh, S.; Faraon, A.; Moerner, W. E. Removing orientation-induced localization biases in single-molecule microscopy using a broadband metasurface mask. *Nature Photonics* **2016**, *10*, 459–462.

(6) Hulleman, C. N.; Thorsen, R. Ø.; Kim, E.; Dekker, C.; Stallinga, S.; Rieger, B. Simultaneous orientation and 3D localization microscopy with a Vortex point spread function. *Nature Communications* **2021**, *12*, 5934.

(7) Hess, S. T.; Girirajan, T. P.; Mason, M. D. Ultra-High Resolution Imaging by Fluorescence Photoactivation Localization Microscopy. *Biophysical Journal* **2006**, *91*, 4258–4272.

(8) Rust, M. J.; Bates, M.; Zhuang, X. Sub-diffraction-limit imaging by stochastic optical reconstruction microscopy (STORM). *Nature Methods* **2006**, *3*, 793–796.

(9) Betzig, E.; Patterson, G. H.; Sougrat, R.; Lindwasser, O. W.; Olenych, S.; Bonifacino, J. S.; Davidson, M. W.; Lippincott-Schwartz, J.; Hess, H. F. Imaging Intracellular Fluorescent Proteins at Nanometer Resolution. *Science* **2006**, *313*, 1642–1645.

(10) Sharonov, A.; Hochstrasser, R. M. Wide-field subdiffraction imaging by accumulated binding of diffusing probes. *Proceedings of the National Academy of Sciences* **2006**, *103*, 18911–18916.

(11) Shaban, H. A.; Valades-Cruz, C. A.; Savatier, J.; Brasselet, S. Polarized super-resolution structural imaging inside amyloid fibrils using Thioflavine T. *Scientific Reports* **2017**, *7*, 12482.

(12) Ding, T.; Wu, T.; Mazidi, H.; Zhang, O.; Lew, M. D. Single-molecule orientation localization microscopy for resolving structural heterogeneities between amyloid fibrils. *Optica* **2020**, *7*, 602–607.

(13) Ding, T.; Lew, M. D. Single-Molecule Localization Microscopy of 3D Orientation and Anisotropic Wobble using a Polarized Vortex Point Spread Function. *bioRxiv* **2021**, 2021.09.13.460135.

(14) Ha, T.; Enderle, T.; Chemla, D. S.; Selvin, P. R.; Weiss, S. Single Molecule Dynamics Studied by Polarization Modulation. *Physical Review Letters* **1996**, *77*, 3979–3982.

(15) Ha, T.; Glass, J.; Enderle, T.; Chemla, D. S.; Weiss, S. Hindered Rotational Diffusion and Rotational Jumps of Single Molecules. *Physical Review Letters* **1998**, *80*, 2093–2096.

(16) Backer, A. S.; Lee, M. Y.; Moerner, W. E. Enhanced DNA imaging using super-resolution microscopy and simultaneous single-molecule orientation measurements. *Optica* **2016**, *3*, 659–666.

(17) Backer, A. S.; Biebricher, A. S.; King, G. A.; Wuite, G. J. L.; Heller, I.; Peterman, E. J. G. Single-molecule polarization microscopy of DNA intercalators sheds light on the structure of S-DNA. *Science Advances* **2019**, *5*, eaav1083.

(18) Mazidi, H.; King, E. S.; Zhang, O.; Nehorai, A.; Lew, M. D. Dense Super-Resolution Imaging of Molecular Orientation Via Joint Sparse Basis Deconvolution and Spatial Pooling. 2019 IEEE 16th International Symposium on Biomedical Imaging (ISBI 2019). 2019; pp 325–329.

(19) Valades Cruz, C. A.; Shaban, H. A.; Kress, A.; Bertaux, N.; Monneret, S.; Mavrakis, M.; Savatier, J.; Brasselet, S. Quantitative nanoscale imaging of orientational order in biological filaments by polarized superresolution microscopy. *Proceedings of the National Academy of Sciences* **2016**, *113*, E820–E828.

(20) Curcio, V.; Alemán-Castañeda, L. A.; Brown, T. G.; Brasselet, S.; Alonso, M. A. Birefringent Fourier filtering for single molecule coordinate and height super-resolution imaging with dithering and orientation. *Nature Communications* **2020**, *11*, 5307.

(21) Rimoli, C. V.; Cruz, C. A. V.; Curcio, V.; Mavrakis, M.; Brasselet, S. 4polar-STORM polarized super-resolution imaging of actin filament organization in cells. *bioRxiv* **2021**, 2021.03.17.435879.

(22) Zhang, O.; Lu, J.; Ding, T.; Lew, M. D. Imaging the three-dimensional orientation and rotational mobility of fluorescent emitters using the Tri-spot point spread function. *Applied Physics Letters* **2018**, *113*, 031103.

(23) Opatovski, N.; Shalev Ezra, Y.; Weiss, L. E.; Ferdman, B.; Orange-Kedem, R.; Shechtman, Y. Multiplexed PSF Engineering for Three-Dimensional Multicolor Particle Tracking. *Nano Letters* **2021**, *21*, 5888–5895.

(24) Zhang, O.; Lew, M. D. Fundamental Limits on Measuring the Rotational Constraint of Single Molecules Using Fluorescence Microscopy. *Physical Review Letters* **2019**, *122*, 198301.

(25) Zhang, O.; Lew, M. D. Quantum limits for precisely estimating the orientation and wobble of dipole emitters. *Physical Review Research* **2020**, *2*, 033114.

(26) Zhang, O.; Lew, M. D. Single-molecule orientation localization microscopy I: fundamental limits. *Journal of the Optical Society of America A* **2021**, *38*, 277.

(27) Backlund, M. P.; Shechtman, Y.; Walsworth, R. L. Fundamental Precision Bounds for Three-Dimensional Optical Localization Microscopy with Poisson Statistics. *Physical Review Letters* **2018**, *121*, 023904.

(28) Tsang, M. Quantum limit to subdiffraction incoherent optical imaging. *Physical Review A* **2019**, *99*, 012305.

(29) Mortensen, K. I.; Churchman, L. S.; Spudich, J. A.; Flyvbjerg, H. Optimized localization analysis for single-molecule tracking and super-resolution microscopy. *Nature Methods* **2010**, *7*, 377–381.

(30) Zhang, O.; Lew, M. D. Single-molecule orientation localization microscopy II: a performance comparison. *Journal of the Optical Society of America A* **2021**, *38*, 288.

(31) Lu, J.; Mazidi, H.; Ding, T.; Zhang, O.; Lew, M. D. Single-Molecule 3D Orientation Imaging Reveals Nanoscale Compositional Heterogeneity in Lipid Membranes. *Angewandte Chemie International Edition* **2020**, *59*, 17572–17579.

(32) Lew, M. D.; Backlund, M. P.; Moerner, W. E. Rotational Mobility of Single Molecules Affects Localization Accuracy in Super-Resolution Fluorescence Microscopy. *Nano Letters* **2013**, *13*, 3967–3972.

(33) Stallinga, S. Effect of rotational diffusion in an orientational potential well on the point spread function of electric dipole emitters. *Journal of the Optical Society of America A* **2015**, *32*, 213.

(34) Chandler, T.; Shroff, H.; Oldenbourg, R.; La Rivière, P. Spatio-angular fluorescence microscopy III Constrained angular diffusion, polarized excitation, and high-NA imaging. *Journal of the Optical Society of America A* **2020**, *37*, 1465.

(35) Sheppard, C. J.; Wilson, T. The image of a single point in microscopes of large numerical aperture. *Proceedings of the Royal Society of London. A. Mathematical and Physical Sciences* **1982**, *379*, 145–158.

(36) Fourkas, J. T. Rapid determination of the three-dimensional orientation of single molecules. *Optics Letters* **2001**, *26*, 211.

(37) Moon, T. K.; Stirling, W. C. *Mathematical Methods and Algorithms for Signal Processing*; Prentice Hall, New Jersey, 2000.

(38) Zhang, Z.; Yomo, D.; Gradinaru, C. Choosing the right fluorophore for single-molecule fluorescence studies in a lipid environment. *Biochimica et Biophysica Acta (BBA) - Biomembranes* **2017**, *1859*, 1242–1253.

(39) Moosaie, A.; Manhart, M. Direct Monte Carlo simulation of turbulent drag reduction by rigid fibers in a channel flow. *Acta Mechanica* **2013**, *224*, 2385–2413.

(40) Novikov, A.; Kuzmin, D.; Ahmadi, O. Random walk methods for Monte Carlo simulations of Brownian diffusion on a sphere. *Applied Mathematics and Computation* **2020**, *364*, 124670.

(41) Halder, A.; Saha, B.; Maity, P.; Kumar, G. S.; Sinha, D. K.; Karmakar, S. Lipid chain saturation and the cholesterol in the phospholipid membrane affect the spectroscopic properties of lipophilic dye nile red. *Spectrochimica Acta Part A: Molecular and Biomolecular Spectroscopy* **2018**, *191*, 104–110.

(42) Huang, Z.; London, E. Effect of Cyclodextrin and Membrane Lipid Structure upon Cyclodextrin–Lipid Interaction. *Langmuir* **2013**, *29*, 14631–14638.

(43) Gharib, R.; Fourmentin, S.; Charcosset, C.; Greige-Gerges, H. Effect of hydroxypropyl-β–cyclodextrin on lipid membrane fluidity, stability and freeze-drying of liposomes. *Journal of Drug Delivery Science and Technology* **2018**, *44*, 101–107.

(44) Ferdman, B.; Nehme, E.; Weiss, L. E.; Orange, R.; Alalouf, O.; Shechtman, Y. VIPR: vectorial implementation of phase retrieval for fast and accurate microscopic pixel-wise pupil estimation. *Optics Express* **2020**, *28*, 10179.